Semi-continuous production of iron oxide nanoparticles via membrane emulsification

*Maria Medina-Llamas and Davide Mattia**

Chemical Engineering Department and Centre for Advanced Separations Engineering, University of Bath, Claverton Down, BA2 7AY Bath, United Kingdom.

***Corresponding author:**
Davide Mattia, **E-mail address:** d.mattia@bath.ac.uk; **telephone:** +44(0)1225-383961

ABSTRACT: The large-scale production of nanomaterials with fine control over their shape, size and properties remains a major obstacle towards their further use. Here, the semi-continuous production of metal oxide nanoparticles (NPs) via membrane emulsification (ME) is reported for the first time, using an *oil-in-water* emulsion and a commercial stirred ME setup fitted with a novel ring-shaped anodic alumina membrane (AAM). A systematic investigation of process parameters showed that the narrow pore size distribution of AAMs resulted in a narrow size distribution of both droplets and particles, with $D_{droplet}/D_{pore}$ as small as 2.8, compared to typical literature values of 10 or more. The average particle size was 4.2 ± 0.5 nm and 18 ± 4 nm for the as-synthetized and calcined NPs, respectively. Calculations of the emulsion production rate demonstrate the potential of the ME setup to produce up to 1 kg of NP per hour per metre squared of membrane.

Keywords: membrane emulsification; nanoemulsions; nanoparticles; hematite; anodic alumina membrane;

1. INTRODUCTION

At the nanoscale, size and shape often determine function, as in the case of iron oxide nanoparticles which switch from ferromagnetic to superparamagnetic below 15 nm [1], or gold, which switches from an inert material to an active catalyst for particle sizes below 5-7 nm [2]. Surface chemistry and crystal structure also do affect properties, for instance anatase becomes more stable than rutile for particle sizes below 14 nm [3]. Thus, the ability to manufacture nanoparticles at a large scale with fine control of their properties is essential to deliver on the promise of nanotechnology to revolutionize a wide range of fields, from medicine to energy to manufacturing [4]. Current nanoparticle synthesis methods can be broadly divided in two categories, wet and dry methods. The former allow inexpensive production at a large scale but with a limited control over properties, as in the case of co-precipitation [5], liquid-liquid interfacial reactions [6], or reverse micelle synthesis [7]. Hydrothermal, solvothermal synthesis and thermal decomposition afford a higher degree of uniformity in morphology [8], but suffer from long reaction times and require moderate to high temperatures [9]. Microwave-assisted synthesis results in the production of monodisperse nanoparticles but is a difficult technology to scale-up due to the limited penetration depth of the radiation into the reaction medium [10]. At the other end of the spectrum are dry methods which, while offering a high degree of property control, require complex equipment which is expensive to scale-up. Examples of these methods include physical vapor deposition [11], laser vaporization [12], non-lithographic templating [13], or thermal plasma synthesis [14]. Consequently, an ideal method would combine the best of both approaches, while also taking into account manufacturing considerations, such as safe operation and waste minimization [4]. Amongst the wet methods for the production of nanoparticles, liquid-liquid reactions at the interface of emulsions combine good morphology control with a

relatively inexpensive process. This is because the reactions to form the particles take place in a confined volume (the emulsion's droplet), with a homogeneous distribution of the reactive species surrounded by the protective layer of the surfactant. An example of this approach is the production of Fe_2O_3 [15], and TiO_2 [16] nanoparticles by reverse micelles. Both examples consisted of small droplets of an aqueous phase surrounded by an organic phase, leading to the formation of *water-in-oil* emulsions. These are ternary systems of water, surfactant and oil that are formed spontaneously under specific conditions of composition and temperature [17]. Under this approach, nanoparticles are usually produced by mixing two phases, one carrying the metal precursor and the other one the reducing agent. The reaction(s) occurs inside the droplets due to the interchange of reactants due to Brownian motion and diffusion. Although the main advantage of this method is the wide range of inorganic salts precursors available, the main drawback relies in the utilization of large amounts of organic solvents as the continuous phase, making the process costly for scale-up and challenging from an environmental and, potentially, a health & safety perspective. A better alternative is the formation of nanoparticles using *oil-in-water* emulsions, with the production of CeO_2, ZrO_2, TiO_2, and ZnO_2 already reported in the literature [18-20].

Despite the advantages described above, the production of nanoparticles from emulsions presents many challenges, primarily due to the method used to produce the emulsions in the first place: Conventional emulsification methods such as rotor-stator, ultrasound systems and high-pressure homogenizers, all produce polydisperse emulsions due to the need to break down the initial coarser emulsion via different disrupting forces (e.g. turbulence, cavitation and shear) [21]. In addition, all of the above methods require significant energy, in the order of $10^6 – 10^8$ J/m^3 [22], most of which is dissipated as heat.

Membrane emulsification (ME), on the other hand, is a scalable, continuous, low energy ($10^4 – 10^6$ J/m^3) emulsification process [22], which can produce large quantities of low dispersity emulsions. This is the result of the droplet formation mechanism, which is less disruptive than the other methods discussed above. In ME, the future dispersed phase permeates through the pores of a membrane, where it meets the continuous phase. A force balance between shear stress induced by the continuous phase flow and interfacial tension, leads to the controlled detachment of droplets [23]. The effect of different process parameters and of the chemistry of both phases is well-understood [24]. Of particular importance to produce droplets with narrow size distribution and, hence, nanoparticles, is the quality of the membrane used, in terms of both pore shape and size. There is a direct relationship between membrane pore diameter, D_p, and droplet size, D_d [24]:

$$D_d = cD_p \quad (1)$$

where c is a proportionality constant. The most commonly used membranes are Shirasu Porous Glass, SPG, a glass-type hydrophilic membrane with interconnected cylindrical pores ranging from 0.05 to 30 μm and reported constant values of c up to 10 [24]. On the other hand, anodic alumina membranes (AAMs), with reported c values ranging from 1.8 to 3.5 have straight pores with constant, circular cross-section [25]. Using these membranes, the authors have produced *oil-in-water* emulsions with droplets as small as 144 ± 18 nm [26]. The small droplet size and narrow size distribution is due to the regular pore structure of the AAMs, which is the result of the manufacturing method, based on the anodization of aluminium [27]. Moreover, their main feature is that the pore diameter can be tuned, from 5 to 200 nm, by altering synthesis conditions such as voltage,

temperature or type of electrolyte [26], while keeping a low porosity (10-20%), making these membranes ideally suited for membrane emulsification [28]. However, these membranes can be brittle and difficult to scale-up.

Hydrophobized AAMs have been used to produce inorganic nanoparticles from *water-in-oil* emulsions, including Ag nanoparticles [29], with kerosene as continuous phase; SiO_2 nanoparticles, using hexane and cyclohexane as continuous phase [30]; and other metal oxides particles with kerosene as continuous phase [31]. However, when producing *water-in-oil* emulsions and using hydrophilic membranes, such as AAMs, the hydrophobization of the membrane is no longer required.

In the present work, the formation of nanoparticles using an *oil-in-water* emulsion via membrane emulsification is presented for the first time. The emulsions are prepared using a semi-continuous process based on the modification of a commercial batch stirred-cell setup, with water as the continuous phase. Hematite nanoparticles were chosen as a model material to due to their use in a wide range of applications, including water splitting, photocatalysis, gas sensors and lithium-ion batteries.

1.1 Membrane emulsification in stirred-cell setup. In this configuration, the dispersed phase is pushed through a flat disk membrane which sits at the bottom of a tank containing the continuous phase. An impeller generates shear in the continuous phase with a radial profile, with the highest value at the critical radius, r_c. [32]:

$$r_c = \frac{D_i}{2} 1.23 \left(0.57 + 0.35 \frac{D_i}{T_D}\right) \left(\frac{b}{T_D}\right)^{0.036} \left(\frac{Re}{1000 + 1.43Re}\right) n_b^{0.116} \quad (2)$$

where D_i is the impeller diameter, T_D is the tank diameter, b is the blade height, n_b is the number of blades. The radial shear stress profile along the membrane leads to the

formation of two regions: the first one for $r \leq r_c$, is a forced vortex region, where the continuous phase exhibits a rigid-body motion with the angular speed of the impeller; the second, is a free vortex region (when $r > r_c$) in which the angular momentum is constant [33]:

$$\tau = 0.825\mu\omega r\frac{1}{\delta} \qquad r \leq r_c \qquad (3)$$

$$\tau = 0.825\mu\omega r\frac{1}{\delta}r_c\left(\frac{r_c}{r}\right)^{0.6} \qquad r > r_c \qquad (4)$$

However, the formation of the radial shear stress profile along the membrane radius leads to the production of droplets with different size depending on the radial position where the droplet is formed, thus leading to the production of an emulsion with wider droplet size distribution. To address this behaviour, metallic ring-shaped membranes in which the porous section is only located in an annulus corresponding to the critical radius have been used to produce emulsions with a smaller coefficient of variation compared to a full membrane with the same pore size [34]. As part of this work, the production of ring-shaped anodic alumina membranes with pores in the nanometre range is also reported for the first time.

2. MATERIALS AND METHODS

2.1 Materials High-purity aluminum foil (99.99%) with 0.25 mm thickness and Iron (III) 2-ethylhexanoate in mineral spirits (Fe 6 %), $Fe(C_8H_{15}O_2)_3$ or $Fe(EH)_3$, used as iron precursor, were purchased from Alfa Aesar. Phosphoric acid (H_3PO_4) 85%, perchloric acid ($HClO_4$) 70%, hydrochloric acid (HCl) 37%, acetone (C_3H_6O) 99%, ethanol (C_2H_5OH) 99%, and copper(II) chloride dihydrated ($CuCl_2{\cdot}2H_2O$) 99%, Tween 20 ($C_{58}H_{114}O_{26}$), Hexane (C_6H_{14}), 28 % wt.

NH_4OH solution and dioctyl sulfosuccinate, commonly named docusate, ($C_{20}H_{37}NaO_7S$), all reactive grade, were purchased from Sigma-Aldrich. Chromium (VI) oxide (CrO_3) 99.5%, oxalic acid anhydrous ($C_2H_2O_4$) 98%, and sulfuric acid (H_2SO_4) 98%, reactive grade, were purchased from Fisher Scientific.

2.2 Synthesis of ring-shape anodic alumina membrane Ring-shaped AAMs were fabricated via a two-step anodization process using a modification of a methodology previously reported [26]. High purity aluminium foil was cut in a circular shape (D= 41 mm). The aluminium piece was annealed in a furnace (Carbolite CWF 1100) at 500 °C for 1 hour, using a temperature ramp of 5 °C min^{-1}. Samples were then degreased in a sonication bath using acetone for 15 minutes. Later, samples were electro-polished to remove the native oxide layer from the Al foil. The procedure was carried out by submerging the sample into a 4:1 solution of 96 % ethanol / 62 % perchloric acid at −77.0 °C ± 5.0 °C under an applied potential of 20 V for 15 minutes. The Al piece was then thoroughly rinsed in ethanol and then water, and placed in a bespoke Teflon holder, leaving an exposed section of foil 26 mm in diameter. The first anodization was then carried out at 60 V using 0.3 M oxalic acid at 10 ˚C for 30 minutes. Next, the Al piece was washed with deionized water and placed in a new set of Teflon holders to remove the first aluminium oxide layer using a 1:1 mixture of 1.8 % wt. H_2CrO_4 / 6 % wt. H_3PO_4 at 60 °C for 25 minutes. Then, the sample was subjected to a second anodization for 6 hours under the same conditions as the first one. To obtain a ringed open porous structure, only the aluminium substrate located beneath the ringed area was exposed to a 1:1 solution of 0.2 M $CuCl_2$ / 20 % wt. HCl, while the rest of the aluminium is protected using a polymeric coating. This procedure lasts until a complete removal of the aluminium in the selected area is achieved and the transparent aluminium oxide porous structure is visible. The final step is the dissolution

of the residual aluminium oxide barrier using a wet chemical method coupled with an electrochemical detection method described elsewhere [25]. Figure S1 in the supporting information show a schematic of the AAM fabrication process.

2.3 Production of emulsions. A batch ME setup (Micropore LDC-1 dispersion cell) was used to produce an *oil-in-water* emulsion by adapting a ring-shaped AAM at the bottom of the setup. The continuous phase consisted of 120 ml of 1.0 % wt. Tween 20 in DI water. The dispersed phase injection line was first filled with continuous phase using a syringe pump until the bottom of the dispersion cell was filled with the continuous phase. The membrane was then placed at the bottom of the dispersion cell, the glass container placed on top of the dispersion cell, followed by an overhead stirrer and the rotational speed adjusted. Next, 2 ml of hexane as dispersed phase were pumped using an injection rate of 0.25 ml/min.

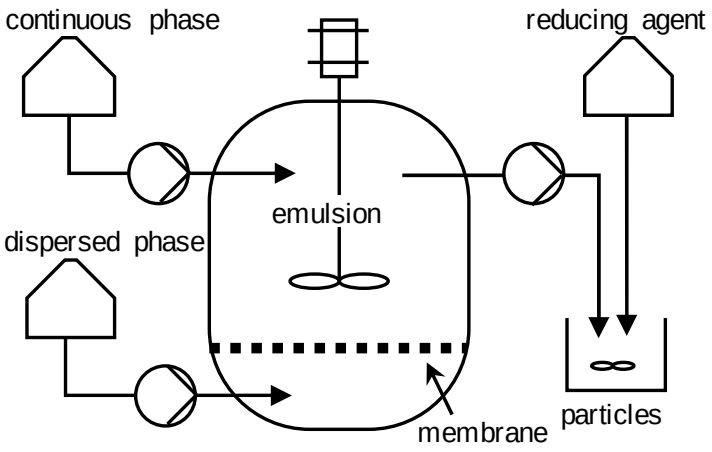

Figure 1. Schematic representation of the semi-continuous membrane dispersion cell to produce hematite nanoparticles via ME. The continuous phase consists of 1.0 % wt. Tween 20 in DI water; the dispersed phase of 60 % v/v $Fe(EH)_3$ in hexane; and the reducing agent (1.5 M NH_4OH).

2.4 Synthesis of nanoparticles. To produce iron oxide nanoparticles, the dispersion cell (Micropore LDC-1) was modified to run as a semi-continuous process, with a constant injection of fresh continuous phase and a constant withdrawal of the emulsion using a double peristaltic pump with a rate of 15 ml/min (Figure 1). This allowed overcoming the limitation represented by the small volume of the commercial cell. The dispersed phase consisted of 17 ml of a 60 % v/v $Fe(EH)_3$ in hexane solution. The continuous phase consisted of 1.5 L of 0.5 % wt. Tween 20 in DI water. 50 ml of 1.5 M NH_4OH were poured into the flask containing the produced emulsion using an injection rate of 1.5 ml/min, while the system was kept under a gentle agitation for 24 h using a magnetic stirrer. The as-produced nanoparticles were then washed using first acetone, then ethanol and finally water in consecutive cycles of centrifugation and sonication four times for each type of solvent. Finally, the nanoparticles were dried at 70 °C for 24 h and calcined at 700 °C using a heating ramp of 5 °C/min and 0.5 hours as dwell time.

2.5 Characterization. FESEM (JEOL JSM 6330F) and TEM (JEOL-JEM-2100 Plus) were used to characterize the AAMs and the hematite nanoparticles, respectively. XRD diffraction patterns of hematite NP were obtained using a Bruker D8-Advance. X-ray photoelectron spectroscopy (XPS) was performed on a ThermoFisher K-alpha+ spectrometer. Samples were analysed using a micro-focused monochromatic Al x-ray source (72 W) over an area of approximately 400 microns. Data was recorded at pass energies of 150 eV for survey scans and 40 eV for high resolution scan with 1 eV and 0.1 eV step sizes respectively. Charge neutralisation of the sample was achieved using a combination of both low energy electrons and argon ions. Data analysis was performed in CasaXPS using a Shirley type background and Scofield cross sections, with an energy dependence of -0.6. All the spectra were calibrated using the C 1s peak with a fixed value

of 284.8 eV. A Raman spectrometer (InVia, Reinshaw) was also used to characterize the iron oxide nanoparticles.

The droplet size distribution of the emulsions was analysed via dynamic light scattering, DLS, with a detection angle of 173° (Zetasizer Nano-ZS, Malvern Instruments). The interfacial tension of the dispersed phase/continuous phase was measured using a goniometer (Dataphysics OCA20) based on the pendant drop method. Statistical image analysis of SEM micrographs of the AAMs and TEM micrographs of the nanoparticles was carried out using *ImageJ t*o obtain the average pore diameter and particle size distribution, respectively. In the case of the AAMs, the software determines the Feret's diameter which is the longest distance between any two tangents contacting the pore edge. Due to the non-perfect circularity of the pores, this results in an overestimation of the pore diameter, which can be compensated by multiplying the Feret's diameter with the pore circularity. Details of this procedure and associated error can be found elsewhere [25].

3. RESULTS AND DISCUSSION

3.1 Ring-shaped anodic alumina membranes. As discussed in the introduction, the shear distribution profile in a stirred cell ME setup leads to the production of droplets with a size distribution. The latter increases with increasing membrane diameter, limiting the maximum size of membrane that can be used without significantly decreasing the quality of the produced emulsion. A solution to this problem has been to develop ring-shaped metallic membranes, with pores, in the micrometre range, present only in an annular section corresponding to the region of maximum shear (as defined by r_c), thereby minimising droplet size variation [34]. In the present work, ring-shaped anodic alumina membranes with pore sizes in the nanometre range have been prepared for the first time with the intention to provide a suitable membrane to

fit a commercial dispersion cell and carry out the production of emulsion with a small droplet size distribution on a larger scale (Figure 2a). The AAMs have straight and non-interconnected pores in a hexagonal arrangement (Figure 2b), with average pore diameter of 77 ± 9 nm and a proportionality constant value of the pore diameter to anodization voltage of 1.30 nm V^{-1}. The average interpore distance is 156 ± 6 nm, giving a proportionality constant value of 2.60 nm V^{-1}. These values are in good agreement with reported values of 1.29 nm V^{-1} and 2.50 nm V^{-1} for pore diameter and interpore distance, respectively [27]. The pore size distributions expressed as percentage of pore frequency can be found in Figure S2. The results show the high degree of pore regularity that can be achieved using 60 V as anodization potential. However, the micrographs also show the formation of a small number of defects (e.g. the formation of slightly elongated pores) which are the result of pore growth competition at early stages of the anodization (Figure 2b).

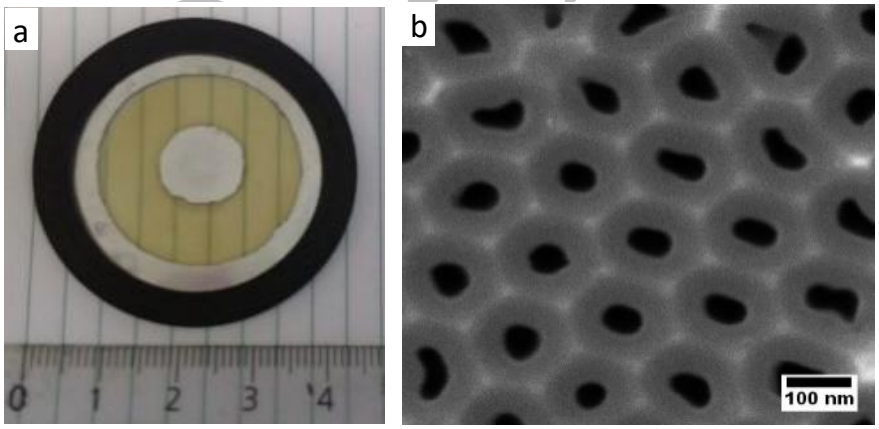

Figure 2. a) Ring-shaped anodic alumina membrane with a black viton o-ring; and b) SEM micrograph of the porous section -the transparent section in a.

Values for pore circularity, pore density and porosity obtained from the statistical image analysis of the FESEM micrographs can be found in Table S1. A SEM micrograph of the

transition zone between the aluminium support and the aluminium oxide porous section shows the formation of surface irregularities with an average extension of 14 ± 3 μm (Figure S3), compared to a membrane diameter of 41 mm. A potential explanation for the formation of this transition zone is the imperfect removal of the aluminium oxide layer during the first anodization as the edge of the membrane holders doesn't ensure a perfect seal between the H_3PO_4/H_2CrO_4 solution and the aluminium oxide located at the edge of the holder. While small, the presence of this region could nonetheless induce the formation of larger droplets or provide a contact surface for multiple droplets to coalesce.

3.2 Emulsion formation. Interfacial tension (IFT) measurements of hexane/water were carried out at different surfactant concentrations (Figure S4). Tween 20 was selected as the surfactant in the continuous phase as is a widely used in ME due to its non-ionic nature [35, 36]. Four repetitions for each experimental condition were carried out at constant temperature of 18 ± 1 ˚C. The results show that for Tween 20 concentrations higher than 1.0 %, the equilibrium IFT has been reached (8.0 ± 0.1 mN/m). This is consistent with results for 1 μm SPG membranes where the minimum droplet size was achieved for Tween 20 concentrations above 0.4 % wt [35]. However, the slow adsorption kinetics of Tween 20 at the hexane/water interface, due to a combined effect of its high molecular weight (1228 g/mol) and its non-ionic nature [37], can result in broadening of average droplet size and widening of its distribution, especially for membranes with small interpore distance values (in the present case equal to 156 ± 6 nm). Therefore, the incorporation of a second surfactant in the dispersed phase was evaluated to induce a faster reduction of the interfacial tension force. The addition of the hydrophobic

surfactant dioctyl sulfosuccinate, commonly named docusate, ($C_{20}H_{37}NaO_7S$), allowed a further reduction of the IFT down to 1.80 mN/m when 1 % wt. was added to the dispersed phase.

Figure 3a and Figure 3b compares the emulsions droplet size distribution at the lowest and highest rotational speed tested, 250 and 1250 rpm, under both surfactant conditions, respectively. At 250 rpm, the results show a single peak at 489 ± 127 nm, when only 1 % wt. Tween 20 in the continuous phase is used, while a peak at 373 ± 64 nm is obtained when both surfactants were added. In contrast, at 1250 rpm narrower droplet size distributions are obtained for both conditions: 230 ± 36 nm (1 % Tween 20 in DI water) and 215 ± 17 nm (1 % Tween 20 in DI water/1 % Docusate in hexane). Figure 3c compares the average size distribution of the emulsion produced at 1250 rpm using both surfactants with the one produced at 1000 rpm, with an average droplet size of 206 ± 21 nm. The proportionality constant values are 2.7 and 2.8, respectively, an indication of the high regularity of the membrane. The values are comparable and show that there is no significant gain in increasing the rotational speed beyond 1000 rpm. The droplet diameter obtained for the complete range of rotational speeds for a 60 V membrane (average pore diameter 77 ± 9 nm) with and without the addition of a surfactant in the dispersed phase can be found in Figure 3d. The effect of the addition of a second surfactant is clearly visible at low rotational speeds, 100 - 500 rpm, where a considerable difference between the average droplet size for both conditions is obtained. The former behaviour is attributed to the drag force not being high enough to produce droplet detachment. The addition of docusate in the system decreases the interfacial tension rate faster than when only a surfactant in the continuous phase is added, although above 1000 rpm, its effect becomes minimal. This can be attributed to the fact that above this value, the droplet size becomes independent of the

shear stress and pore diameter is the main parameter that determines the droplet diameter [26]. Above 1000 rpm, the average droplet diameter to pore diameter is approximately 2.8 (Figure 3e), an indication of the high regularity of the membranes produced, compared to values up to 10 for SPG membranes [24]. In addition, the proportionality constant values are in good agreement with a previous publication on the production of emulsions using a fully open porous AAM.[26]

The dependence of the droplet diameter on the rotational speed can be evaluated quantitatively in terms of a force balance using the Euler number. This dimensionless number is the ratio of pressure to inertial forces, the former determined by the injection of the dispersed phase and the latter from the rotational speed of the continuous phase [26, 38]:

$$Eu = \frac{\Delta P}{\rho_c N^2 D_i^2} = \frac{4\gamma}{\rho_c N^2 D_i^2 D_p^2} \quad (5)$$

where ρ_c is the density of the continuous phase, D_i is the diameter of the impeller (3.1 cm, see Figure 1), N the rotational speed in revolutions per second and γ the IFT. This dependence for an emulsion produced using an AMM with average pore diameter of 77 ± 9 nm is shown in Figure 3f: For a constant dispersed phase injection rate, an increase in the rotational speed of the impeller leads to an increase in shear (hence a higher Eu number) and a smaller D_d/D_p ratio.

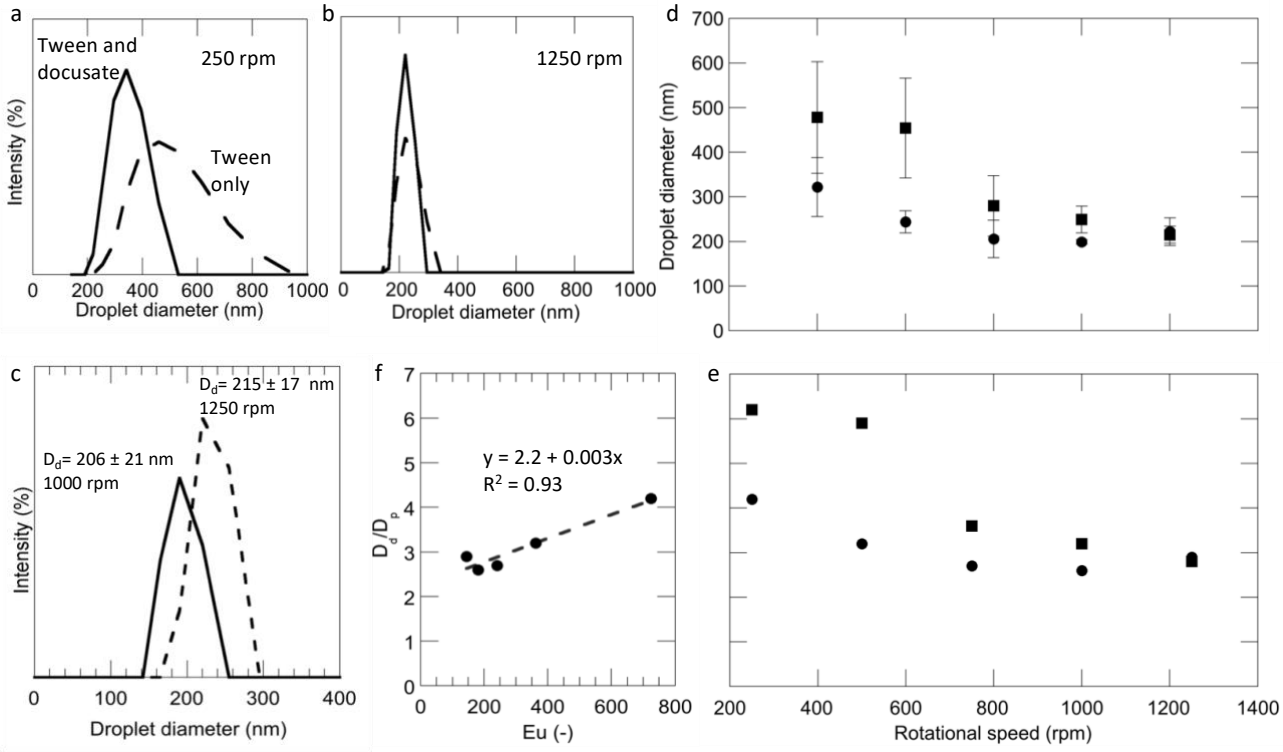

Figure 3. Intensity vs. droplet diameter for emulsions produced using 1 % wt. Tween 20 in DI Water as continuous phase and with and without the incorporation of surfactant (1% wt. Docusate) in the dispersed phase (hexane) at rotational speeds of a) 250 rpm and b) 1250 rpm; c) droplet size distribution of emulsion produced at 1000 and 1250 rpm; d) emulsion droplet size and e) ratio of droplet diameter to pore diameter vs. rotational speed, with 1 % wt. Tween 20 in DI water and with (●) and without (■) the incorporation of 1 % wt. docusate in dispersed phase (hexane); and f) ratio of droplet diameter to pore diameter vs. Euler number for an emulsion produced for all rotational speeds investigated.

The radial position of the porous section of the ring-shaped AAMs is from 6 mm < r < 14 mm (Figure 2a) and has an effective membrane area of ~ 503 mm^2. Based on Eq. 2, the

position of the critical radius is located between 10 to 11 mm for 250 and 1250 rpm, respectively. The value of the shear stress at the critical radius, allows estimating the average droplet size using the following droplet size estimation model:[39]

$$\left[6k_x\pi\tau h^2 + \frac{4}{3}\pi r^3(\rho_c - \rho_d)g\right]h = 2\pi\gamma r_p^2 \tag{6}$$

$$\frac{4}{3}\pi r^3 = \frac{\pi}{6}h\left(3r_p^2 + h^2\right) \tag{7}$$

where k_x is the wall correction factor, h is droplet height, r is radius droplet, g is gravitational constant, r_p is the pore radius, ρ_c and ρ_d are the density of the continuous and dispersed phase, respectively.

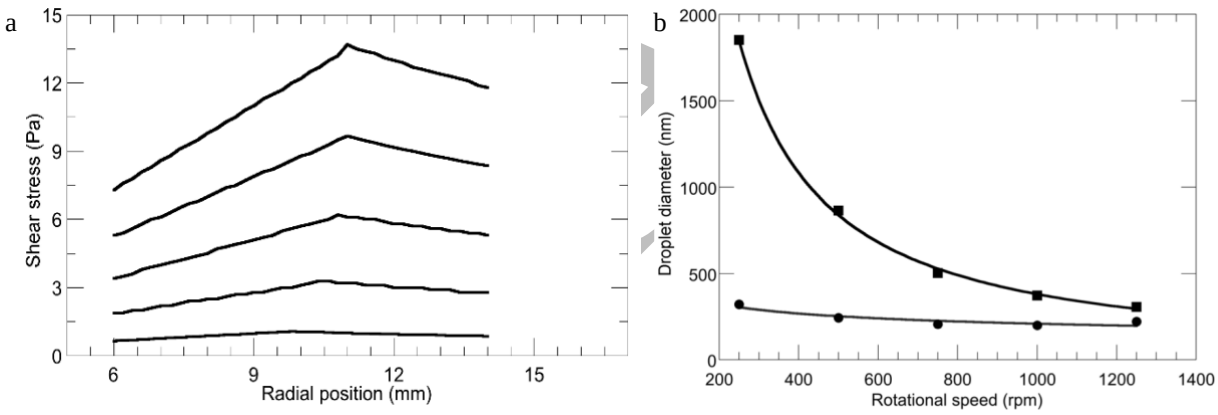

Figure 4. a) Shear stress profile against radius at the porous section of the ring-shaped AAM for different rotational speeds b) comparison of the experimental droplet diameter and estimated droplet diameter at the critical radius.

Figure 4a shows the shear stress varies along the membrane's diameter, increasing from the centre outwards until it reaches a maximum (at the critical radius) [39] in the middle of

the porous ring section. The value of the shear stress at the critical radius can then be used to estimate the average droplet size [39]. The results in Figure 4b show the predicted values tend to converge at higher rotational speeds, with an overestimation at 1250 rpm of ~22 %. While this value might appear large, the authors have previously shown that other models available in the literature and derived for micrometre emulsion droplets can lead to overestimation of up to 600 % [26].

3.3 Nanoparticle formation. From Figure 3d, it was observed that the smallest droplet size was produced at rotational speeds above 1000 rpm. Therefore, the synthesis of hematite nanoparticles was carried out using bespoke ring-shaped AAMs at rotational speeds higher than 1000 rpm. The synthesis of iron oxide nanoparticles was carried out for the two highest rotational speed and the particles were first analysed by TEM. Figure 5a show the micrograph of the as-synthetized iron oxide nanoparticles, giving an average particle size of 3.7 ± 1 nm and 4.2 ± 0.5 nm for the nanoparticles nm synthetized at 1000 and 1250 rpm, respectively. A FFT analysis of the TEM micrographs showed the formation of nanoparticles in direction of the planes (024) and (113) with an interplanar distance of 0.19 nm and 0.22 nm, respectively. The difference in the nanoparticle diameter for the two rotational speeds is within the error, with no meaningful difference between the two. As only a minimal reduction in the particle size was achieved by varying the rotational speed, further iron oxide nanoparticles were produced using 1000 rpm. The as-synthesized particles are about 2 orders of magnitude smaller than the starting droplets. This large size reduction is well-known and can be ascribed to two factors, the low concertation of reactant in the dispersed phase and the shrinkage when such reactant is reduced from salt ion to solid particle [18-20]. While there is no known fundamental relationship between

the two, the results obtained here are consistent with those obtained in the literature for metal oxide particles obtained from *water-in-oil* emulsion [29, 30]. It should be added that the relatively low concentration of reactant in the dispersed phase is not an impediment to the large-scale production of particles as the latter is really a function of how many particles can be produced, i.e. how many droplets are produced. On the other hand, the fact that the reaction is self-limited by the amount of reactant present in the droplets, combined with the narrow droplet size distribution afforded by using AAMs with narrow pore size distribution, leads to the very narrow particle size distributions obtained here.

The as-synthesized nanoparticles were then calcined at 700 °C, to ensure the formation of hematite. Calcination promoted grain boundary enlargement due to the high surface energy of the nanocrystalline nanoparticles and thus an increase in the nanoparticle size was observed [40], with the average particle size for the calcined nanoparticles being 18 ± 4 nm (Figure 5b). In this case, the FFT showed the formation of nanoparticles in the direction of the planes (024), (113), (110) and (104) with an interplanar distance of 0.19, 0.22, 0.25 and 0.27 nm, respectively, which are characteristic of hematite [41]. Higher resolution TEM of individual calcined particles confirm the crystalline structure of hematite (Figure S5).

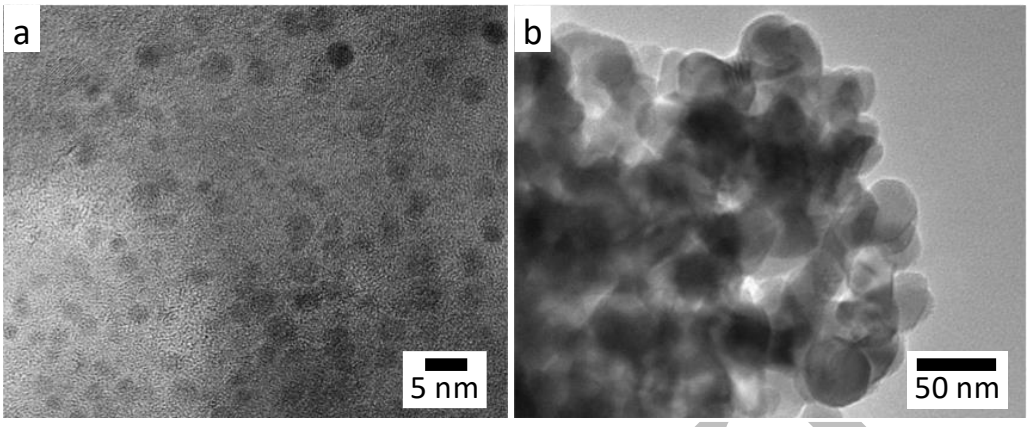

Figure 5. TEM micrographs of hematite nanoparticles a) as-synthesized and b) calcined at 700° C.

The XRD pattern of the calcined nanoparticles (Figure 6a) confirms the formation of hematite (JCPDS cards 13-0534). The average particle size deduced using the Scherrer equation of the two strongest peaks (104) and (110) is 25 nm, slightly larger than the TEM values. Figure 6b shows the Raman spectrum of the as-synthetized and calcined iron oxide nanoparticles with distinctive Raman frequencies for hematite. The Raman frequencies at 227, 293, 412 and 612 cm^{-1} correspond to the E_g modes, in good agreement with the literature [42]. The bands at 227 and 498 cm^{-1} are assigned to A_{1g} modes [43]. The as-synthetized nanoparticles have broader Raman frequencies with values shifted to lower wavenumbers due to their smaller particle size [44]. Additionally, the Raman spectra of hematite exhibit an extra line at about 660 cm^{-1}, and the apparition of a shoulder at 412 cm^{-1} which are more pronounced for the smaller particles [43]. The former lines are consistent with the Raman spectrum of the as-synthetized nanoparticles.

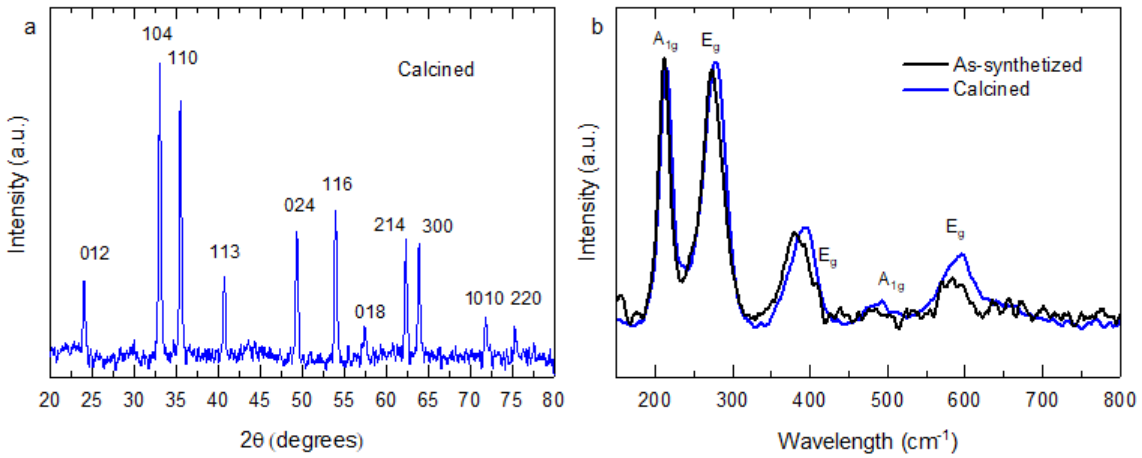

Figure 6. a) X-Ray diffraction pattern of hematite nanoparticles calcined at 700° C b) Raman spectra of the as-synthetized and calcined iron oxide nanoparticles

XPS analysis was conducted to further investigate the composition and bonding of the iron oxide nanoparticles. The global XPS profile for all the samples is shown in Figure 7a. The results show the incorporation of sodium and carbon within the iron oxide matrix. The former comes from the surfactant (Docusate), while the latter is likely to originate from the hexane of the dispersed phase. For a further analysis, the chemical structure of both iron oxide samples is examined in four specific areas of the XPS spectrum.

Figure 7b shows the iron core level region for the as-synthesised and calcined samples. The characteristic peaks for hematite are clearly visible for both samples at 710.8 (Fe $2p_{3/2}$) and 724 (Fe $2p_{1/2}$), with their respective shake-up satellites are at 718 and 732 eV [45]. The peak separation between the Fe 2p peaks and their respective satellites is 8 eV, which indicates iron atoms have +3 as oxidation state.[46] Figure S6e shows the characteristic peaks for hematite at 93 eV (Fe 3s) and 55 eV (Fe $3p_{3/2}$) [47]. The deconvolution of the Fe

$2p_{3/2}$ peak with its satellite (Figure S6c and Figure S6d) shows that the broader peak at 710.3 eV, is close to the reported binding energy value for hematite (Table S2) [48-50].

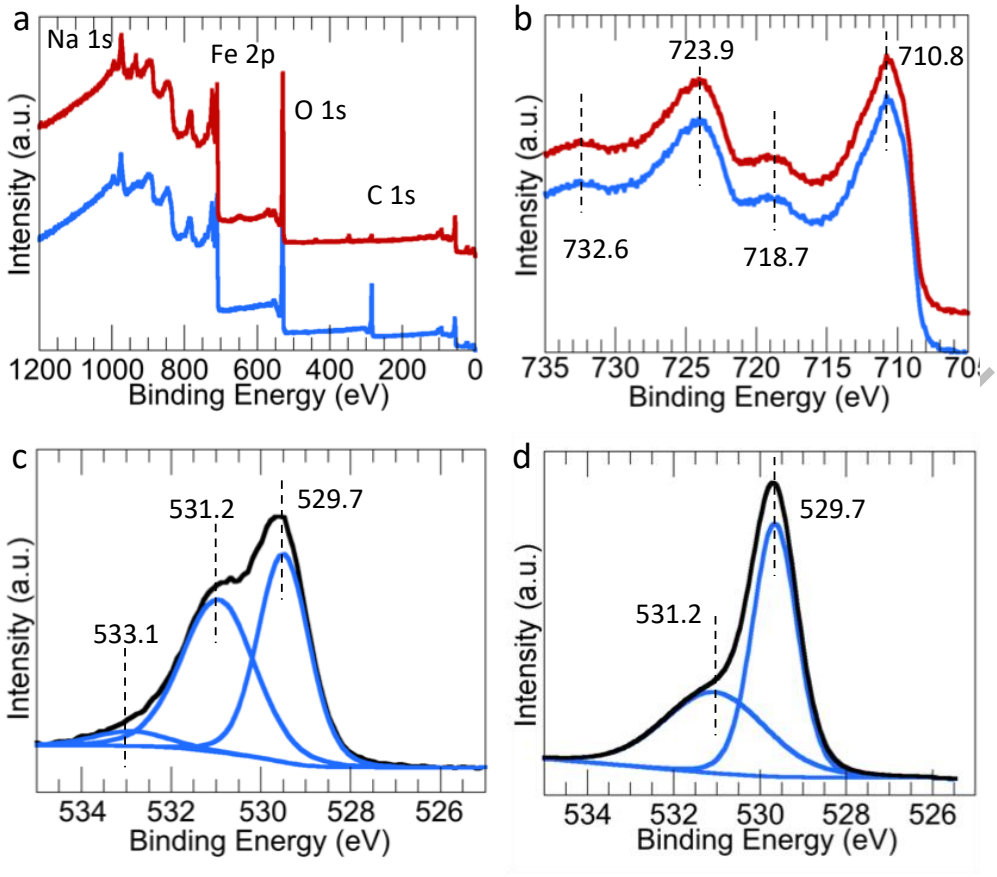

Figure 7. a) Global XPS analysis of the iron oxide nanoparticles for the as- synthetized (-) and the calcined sample (-), high resolution analysis of the b) Fe 2p region, O 1s core level for the c) as-synthetized and d) calcined sample.

The O 1s core level region (Figure 7c and Figure 7d) shows that the as-synthetized samples not only have the characteristic peak for the O^{2-} from hematite with binding energy (BE) of 529 eV [41], but also two other peaks, one at 531 eV, which can be attributed to the presence of hydroxyl species over the surface of the iron oxide [51], originated from the addition of NH_4OH during synthesis, and one at 533 eV which indicates the presence of

absorbed water molecules [52]. This latter peak is absent from the calcined samples, whereas the hydroxyl one is significantly attenuated. The C 1s core level (Figure S6a and Figure S6b) show the first peak at 284 eV is associated with carbon on the surface due to the nature of the iron precursor and the dispersed phase. The peaks at 286 and 288 eV are due to oxidized carbon species C – O and COOH, respectively [53]. The first peak is associated with carbon residues on the iron oxide surface from the surfactant, while the second peak is due to carboxylic groups from the organometallic precursor [54]. In conclusion, TEM, XRD, Raman and XPS all conclusively show the formation of hematite nanoparticles after calcination.

3.4 Productivity and scale-up. The productivity of the particle production was calculated starting from the flow rate of the dispersed phase, the amount of iron ions in the dispersed phase and the area of the porous section of the membrane. Assuming (i) that each droplet will convert into one hematite nanoparticle, and (ii) 100% conversion of iron to hematite as per the reaction $\boldsymbol{2Fe^{3+} + 6OH^{-} \rightarrow Fe_2O_3 + 3H_2O}$, the mass of hematite nanoparticles particles produced in one hour per m^2 of membrane is equal to ~1.4 kg h^{-1} m^{-2}. Details of the calculations can be found in Table S3. Assuming there will be losses associated to fouling or agglomeration, a more conservative production rate of 1 kg of nanoparticles per hour per m^2 of membrane is assume here. Nonetheless, such a value for the production rate of nanoparticle with the narrow size distribution shown here would open the way to the large-scale manufacturing of nanoparticles with fine control over their properties.

4. Conclusions

Hematite nanoparticles were synthetized using a semi-continuous ME process. The setup consisted of a commercial available stirred-cell to which a bespoke ring-shape AAM was fitted (D_p = 77 ± 9 nm) to produce an *oil-in-water* emulsion. The dispersed phase consisted of iron (III) 2-ethylhexanoate in 1 % docusate in hexane, while the continuous phase consisted of 1 % Tween 20 in DI water. The effect of the rotational speed over the droplet size and size distribution was evaluated. The results show the formation of emulsions droplets small as 206 ± 21 nm at 1000 rpm, while values of the ratio $D_{droplet}/D_{pore}$ were ranging from 2.8 to 6.2. As-produced and calcined iron oxide nanoparticles were characterized by TEM, XRD, Raman and XPS. The results revealed the formation of hematite with particle size of ~4 nm for the as-synthetized sample and ~18 nm for the calcined samples. To the authors' knoweldge, this is the first report on the production of metal oxide nanoparticles using a scalable, oil-in-water membrane emulsfication process that can be easily scaled-up. Based on the calculation of the nanoparticle production rate, this manufacturing method can produce up to 1 kg of nanoparticles per hour per metre square of membrane with a fine control of the particle size.

ASSOCIATED CONTENT

Supporting Information

Scheme of the fabrication of ring-shaped AAMs (Figure S1), pore size distribution by frequency for a 60 V ring-shaped AAM (Figure S2), statistical parameters obtained by ImageJ from the ring-shaped AAM (Table S1), Transition zone between the porous alumina layer and the aluminium support in a ring-shaped AAM (Figure S3), IFT hexane/water at different surfactant concentrations (Tween 20) in the continuous phase (Figure S4), High resolution TEM micrographs of calcined hematite nanoparticles (Figure S5); High resolution profile by X-ray

photon spectroscopy for the C 1s core level of the, Fe $2p_{3/2}$ core level and Fe 3s (93 eV) and Fe $3p_{3/2}$ (55 eV) levels for the as-synthetized and calcined samples (Figure S6), Fe $2p_{3/2}$ spectral fitting parameters: binding energy, percentage of total area, FWHM value (Table S2), Productivity calculations for hematite NP by ME (Table S3). All data created during this research are openly available from the University of Bath data archive at https://doi.org/10.15125/BATH-00544

AUTHOR INFORMATION

Corresponding Author

*E-mail: dmattia@bath.ac.uk

Notes

The authors declare no competing financial interest.

ACKNOWLEDGEMENTS

The authors express their gratitude to the Mexican National Council for Science and Technology (CONACYT) for the doctoral scholarship granted to M.M.-L. XPS data collection was performed at the EPSRC National Facility for XPS ('HarwellXPS'), operated by Cardiff University and UCL, under contract No. PR16195.

ABBREVIATIONS

AAMs = anodic alumina membranes

DI = deionized water

DLS = dynamic light scattering

FESEM = Field emission scanning electron microscope

FWHM = full width half maximum

IFT =Interfacial tension force

ME = membrane emulsification

TEM = transmission electron microscope

XPS = X-ray photoelectron spectroscopy

XRD = X-ray diffraction spectroscopy

Nomenclature

A_{mem} = membrane area (m^2)

b = blade height (m)

c = proportionality constant between droplet diameter and pore diameter (−)

D_i = impeller diameter (m)

D_d = droplet diameter (m)

D_p = pore diameter (m)

Eu = Euler number (−)

g = gravitational constant (9.81 m s^{-2})

h = droplet height (m)

k_x = wall correction factor (−)

$\dot{m}_{Fe(EH)_3}$ = mass flow rate of $Fe(EH)_3$ (g min^{-1})

$\dot{m}_{Fe_2O_3}$ = mass flow rate of Fe_2O_3 (g min^{-1})

N = rotational speed (rps)

n_b = number of blades (−)

ΔP = transmembrane pressure (Pa)

Q_{disp} = flow rate of the dispersed phase (m^3 min^{-1})

r_c = critical radius (m)

r_d = droplet radius (m)

r_p = membrane pore radius (m)

Re = Reynolds number (−)

T_D = tank diameter (m)

Symbols

γ = interfacial tension (mN m^{-1})

δ = boundary layer thickness (m)

ρ_c = density of the continuous phase (kg m^{-3})

ρ_d = density of the dispersed phase (kg m^{-3})

τ = shear stress (Pa)

ω = angular speed of the impeller (rad s^{-1})

REFERENCES

[1] J. Chatterjee, Y. Haik, C.-J. Chen, Size dependent magnetic properties of iron oxide nanoparticles, J. Magn. Magn. Mater. 257(1) (2003) 113-118.
[2] T.V. Janssens, B.S. Clausen, B. Hvolbæk, H. Falsig, C.H. Christensen, T. Bligaard, J.K. Nørskov, Insights into the reactivity of supported Au nanoparticles: combining theory and experiments, Topics in Catalysis 44(1) (2007) 15-26.
[3] H. Zhang, J.F. Banfield, Size dependence of the kinetic rate constant for phase transformation in TiO2 nanoparticles, Chem. Mater. 17(13) (2005) 3421-3425.
[4] A. Dowling, R. Clift, N. Grobert, D. Hutton, R. Oliver, O. O'Neill, J. Pethica, N. Pidgeon, J. Porritt, J. Ryan, Nanoscience and nanotechnologies: opportunities and uncertainties. Royal Society and Royal Academy of Engineering, London, UK, 2004.

[5] R. Valenzuela, M.C. Fuentes, C. Parra, J. Baeza, N. Duran, S. Sharma, M. Knobel, J. Freer, Influence of stirring velocity on the synthesis of magnetite nanoparticles (Fe 3 O 4) by the co-precipitation method, J. Alloys Compd. 488(1) (2009) 227-231.
[6] C. Rao, K. Kalyanikutty, The liquid–liquid interface as a medium to generate nanocrystalline films of inorganic materials, Acc. Chem. Res. 41(4) (2008) 489-499.
[7] D. Zhang, L. Qi, J. Ma, H. Cheng, Formation of crystalline nanosized titania in reverse micelles at room temperature, J. Mater. Chem. 12(12) (2002) 3677-3680.
[8] J. Cai, Y.Q. Miao, B.Z. Yu, P. Ma, L. Li, H.M. Fan, Large-Scale, Facile Transfer of Oleic Acid-Stabilized Iron Oxide Nanoparticles to the Aqueous Phase for Biological Applications, Langmuir 33(7) (2017) 1662-1669.
[9] L. Diamandescu, D. Mihaila-Tarabasanu, N. Popescu-Pogrion, A. Totovina, I. Bibicu, Hydrothermal synthesis and characterization of some polycrystalline α-iron oxides, Ceram. Int. 25(8) (1999) 689-692.
[10] X. Liao, J. Zhu, W. Zhong, H.-Y. Chen, Synthesis of amorphous Fe 2 O 3 nanoparticles by microwave irradiation, Mater. Lett. 50(5) (2001) 341-346.
[11] B. Xiang, Y. Zhang, Z. Wang, X. Luo, Y. Zhu, H. Zhang, D. Yu, Field-emission properties of TiO2 nanowire arrays, J. Phys. D: Appl. Phys. 38(8) (2005) 1152.
[12] U. Lohbauer, A. Wagner, R. Belli, C. Stoetzel, A. Hilpert, H.-D. Kurland, J. Grabow, F.A. Müller, Zirconia nanoparticles prepared by laser vaporization as fillers for dental adhesives, Acta Biomater. 6(12) (2010) 4539-4546.
[13] Highly ordered CdS nanoparticle arrays on silicon substrates and photoluminescence properties, Applied Physics Letters 86(10) (2005) 103106.
[14] H.-F. Lin, S.-C. Liao, S.-W. Hung, The dc thermal plasma synthesis of ZnO nanoparticles for visible-light photocatalyst, J. Photochem. Photobiol. A: Chem. 174(1) (2005) 82-87.
[15] J. Shi, H. Verweij, Synthesis and purification of oxide nanoparticle dispersions by modified emulsion precipitation, Langmuir 21(12) (2005) 5570-5575.
[16] M.S. Lee, S.S. Park, G.-D. Lee, C.-S. Ju, S.-S. Hong, Synthesis of TiO 2 particles by reverse microemulsion method using nonionic surfactants with different hydrophilic and hydrophobic group and their photocatalytic activity, Catal. Today 101(3) (2005) 283-290.
[17] T. Hellweg, Phase structures of microemulsions, Current Opinion in Colloid & Interface Science 7(1–2) (2002) 50-56.
[18] K. Pemartin, C. Solans, G. Vidal-Lopez, M. Sanchez-Dominguez, Synthesis of ZnO and ZnO2 nanoparticles by the oil-in-water microemulsion reaction method, Chem. Lett. 41(10) (2012) 1032-1034.
[19] M. Sanchez-Dominguez, L.F. Liotta, G. Di Carlo, G. Pantaleo, A.M. Venezia, C. Solans, M. Boutonnet, Synthesis of CeO2, ZrO2, Ce0. 5Zr0. 5O2, and TiO2 nanoparticles by a novel oil-in-water microemulsion reaction method and their use as catalyst support for CO oxidation, Catal. Today 158(1-2) (2010) 35-43.
[20] C. Tiseanu, B. Cojocaru, V.I. Parvulescu, M. Sanchez-Dominguez, P.A. Primus, M. Boutonnet, Order and disorder effects in nano-ZrO 2 investigated by micro-Raman and spectrally and temporarily resolved photoluminescence, PCCP 14(37) (2012) 12970-12981.
[21] E. Piacentini, A. Figoli, L. Giorno, E. Drioli, 4.03 - Membrane Emulsification, Comprehensive Membrane Science and Engineering, Elsevier, Oxford, 2010, pp. 47-78.
[22] H. Schubert, R. Engel, Product and Formulation Engineering of Emulsions, Chem. Eng. Res. Des. 82(9) (2004) 1137-1143.

[23] S. Peng, R.A. Williams, Controlled Production of Emulsions Using a Crossflow Membrane, Particle & Particle Systems Characterization 15(1) (1998) 21-25.
[24] C. Charcosset, I. Limayem, H. Fessi, The membrane emulsification process—a review, Journal of Chemical Technology & Biotechnology 79(3) (2004) 209-218.
[25] K.P. Lee, H. Leese, D. Mattia, Water flow enhancement in hydrophilic nanochannels, Nanoscale 4(8) (2012) 2621-2627.
[26] M. Medina-Llamas, D. Mattia, Production of Nanoemulsions Using Anodic Alumina Membranes in a Stirred-Cell Setup, Industrial & Engineering Chemistry Research (2017).
[27] J. O'sullivan, G. Wood, The morphology and mechanism of formation of porous anodic films on aluminium, P. Roy. Soc Lond. A. 317(1531) (1970) 511-543.
[28] H. Leese, V. Bhurtun, K.P. Lee, D. Mattia, Wetting Behaviour of Hydrophilic and Hydrophobic Nanostructured Porous Anodic Alumina, Colloids and Surfaces A: Physicochemical and Engineering Aspects 420(0) (2013) 53-58.
[29] E. Kakazu, T. Murakami, K. Akamatsu, T. Sugawara, R. Kikuchi, S.-i. Nakao, Preparation of silver nanoparticles using the SPG membrane emulsification technique, Journal of Membrane Science 354(1-2) (2010) 1-5.
[30] T. Yanagishita, Y. Tomabechi, K. Nishio, H. Masuda, Preparation of Monodisperse SiO2 Nanoparticles by Membrane Emulsification Using Ideally Ordered Anodic Porous Alumina, Langmuir 20(3) (2004) 554-555.
[31] T. Yanagishita, Y. Maejima, K. Nishio, H. Masuda, Monodisperse nanoparticles of metal oxides prepared by membrane emulsification using ordered anodic porous alumina, RSC Advances 4(4) (2014) 1538-1542.
[32] S. Nagata, Mixing: principles and applications, Halsted Press1975.
[33] S.R. Kosvintsev, G. Gasparini, R.G. Holdich, I.W. Cumming, M.T. Stillwell, Liquid-liquid membrane dispersion in a stirred cell with and without controlled shear, Ind. Eng. Chem. Res. 44(24) (2005) 9323-9330.
[34] M.T. Stillwell, R.G. Holdich, S.R. Kosvintsev, G. Gasparini, I.W. Cumming, Stirred cell membrane emulsification and factors influencing dispersion drop size and uniformity, Ind. Eng. Chem. Res. 46(3) (2007) 965-972.
[35] R. Hancocks, F. Spyropoulos, I. Norton, Comparisons between membranes for use in cross flow membrane emulsification, J. Food Eng. 116(2) (2013) 382-389.
[36] P. Thanasukarn, R. Pongsawatmanit, D.J. McClements, Influence of emulsifier type on freeze-thaw stability of hydrogenated palm oil-in-water emulsions, Food Hydrocolloids 18(6) (2004) 1033-1043.
[37] M. Rayner, G. Trägårdh, C. Trägårdh, The impact of mass transfer and interfacial expansion rate on droplet size in membrane emulsification processes, Colloids Surf. Physicochem. Eng. Aspects 266(1) (2005) 1-17.
[38] M.A. Suárez, G. Gutiérrez, M. Matos, J. Coca, C. Pazos, Emulsification using tubular metallic membranes, Chem. Eng. Process. Process Intensif. 81 (2014) 24-34.
[39] K.P. Lee, D. Mattia, Manufacturing of Nanoemulsions Using Nanoporous Anodized Alumina Membranes: Experimental Investigation and Process Modeling, Ind. Eng. Chem. Res. 52(42) (2013) 14866-14874.
[40] S. Shukla, S. Seal, R. Vij, S. Bandyopadhyay, Reduced activation energy for grain growth in nanocrystalline yttria-stabilized zirconia, Nano Lett. 3(3) (2003) 397-401.
[41] R.M. Cornell, U. Schwertmann, The iron oxides: structure, properties, reactions, occurrences and uses, John Wiley & Sons2003.

[42] D. De Faria, F. Lopes, Heated goethite and natural hematite: can Raman spectroscopy be used to differentiate them?, Vibrational Spectroscopy 45(2) (2007) 117-121.
[43] I. Chernyshova, M. Hochella Jr, A. Madden, Size-dependent structural transformations of hematite nanoparticles. 1. Phase transition, PCCP 9(14) (2007) 1736-1750.
[44] W.B. White, Structure of Particles and the Structure of Crystals: Information from Vibrational Spectroscopy, Journal of Ceramic Processing & Research 6(1) (2005) 1-9.
[45] T. Yamashita, P. Hayes, Analysis of XPS spectra of Fe2+ and Fe3+ ions in oxide materials, Appl. Surf. Sci. 254(8) (2008) 2441-2449.
[46] M. Descostes, F. Mercier, N. Thromat, C. Beaucaire, M. Gautier-Soyer, Use of XPS in the determination of chemical environment and oxidation state of iron and sulfur samples: constitution of a data basis in binding energies for Fe and S reference compounds and applications to the evidence of surface species of an oxidized pyrite in a carbonate medium, Appl. Surf. Sci. 165(4) (2000) 288-302.
[47] J. Desai, H. Pathan, S.-K. Min, K.-D. Jung, O.S. Joo, FT-IR, XPS and PEC characterization of spray deposited hematite thin films, Appl. Surf. Sci. 252(5) (2005) 1870-1875.
[48] A. Grosvenor, B. Kobe, M. Biesinger, N. McIntyre, Investigation of multiplet splitting of Fe 2p XPS spectra and bonding in iron compounds, Surface and Interface Analysis 36(12) (2004) 1564-1574.
[49] K. Wandelt, Photoemission studies of adsorbed oxygen and oxide layers, Surface Science Reports 2(1) (1982) 1-121.
[50] K. Asami, K. Hashimoto, S. Shimodaira, X-ray photoelectron spectrum of Fe2+ state in iron oxides, Corros. Sci. 16(1) (1976) 35-45.
[51] M. Aronniemi, J. Lahtinen, P. Hautojärvi, Characterization of iron oxide thin films, Surface and interface analysis 36(8) (2004) 1004-1006.
[52] A. Grosvenor, B. Kobe, N. McIntyre, Studies of the oxidation of iron by water vapour using X-ray photoelectron spectroscopy and QUASES™, Surf Sci. 572(2-3) (2004) 217-227.
[53] Y. Park, W. Kim, H. Park, T. Tachikawa, T. Majima, W. Choi, Carbon-doped TiO 2 photocatalyst synthesized without using an external carbon precursor and the visible light activity, Applied Catalysis B: Environmental 91(1) (2009) 355-361.
[54] D. Chen, Z. Jiang, J. Geng, Q. Wang, D. Yang, Carbon and nitrogen co-doped TiO2 with enhanced visible-light photocatalytic activity, Ind. Eng. Chem. Res. 46(9) (2007) 2741-2746.